Changing the static and dynamic lattice effects for the improvement of the ionic transport properties within the argyrodite $Li_6PS_{5-x}Se_xI$

Roman Schlem[a,b], Michael Ghidiu[a,b], Sean P. Culver[a,b], Anna-Lena Hansen[c],

Wolfgang G. Zeier*[a,b]

[a]Institute of Physical Chemistry, Justus-Liebig-University Giessen, Heinrich-Buff-Ring 17, D-35392 Giessen, Germany.

[b]Center for Materials Research (LaMa), Justus-Liebig-University Giessen, Heinrich-Buff-Ring 16, D-35392 Giessen, Germany.

[c] Institute for Applied Materials - Energy Storage Systems, Karlsruhe Institute of Technology, Hermann-von-Helmholtz-Platz 1, D-76344 Eggenstein-Leopoldshafen, Germany

Abstract

The lithium argyrodites Li_6PS_5X (X = Cl, Br, I) have been gaining momentum as candidates for electrolytes in all-solid-state batteries. While these materials have been well-characterized structurally, the influences of the static and dynamic lattice properties are not fully understood. Recent improvements to the ionic conductivity of Li_6PS_5I (which as a parent compound is a poor ionic conductor) via elemental substitutions have shown that a multitude of influences affect the ionic transport in the lithium argyrodites, and that even poor conductors in this class have room left for improvement.

Here we explore the influence of isoelectronic substitution of sulfur with selenium in $Li_6PS_{5-x}Se_xI$. Using a combination of X-ray diffraction, impedance spectroscopy, Raman spectroscopy, and pulse-echo speed of sound measurements, we explore the influence of the static and dynamic lattice on the ionic transport. The substitution of S^{2-} with Se^{2-} broadens the diffusion pathways and structural bottlenecks, as well as leading to a softer more polarizable lattice, all of which lower the activation barrier and lead to an increase in the ionic conductivity. This work sheds light on ways to systematically understand and improve the functional properties of this exciting material family.

Keywords: solid electrolyte, lithium argyrodites, lattice dynamics, ionic conductivity, diffusion pathways

1. INTRODUCTION

With the steadily rising demand for safer and higher-density energy storage, all-solid-state batteries have become a major research topic during the last few decades.[1,2] The implementation of solid electrolytes into lithium-ion battery technologies would remove the flammability hazards of organic electrolytes, as well as offer higher mechanical stability and the potential to utilize Li metal electrodes. Nevertheless, this goal remains challenging, partially due to the search for materials with not only high ionic conductivity but that also function well within a device, having the desired morphology, compatibility with the required electrodes, and proper mechanical stability.[3–5] One of the most important issues is the often low ionic conductivity of solid electrolytes, and though much progress has been made on this front, the conductivities can often span several orders of magnitude between seemingly similar (or even seemingly identical) compounds.[6,7]

Prominent compound classes that are being considered are the lithium conducting garnets such as $Li_7La_3Zr_2O_{12}$,[8–11] the Li^+ - NASICON's $LiM_2^{4+}(PO_4)_3$ ($M = Ti^{4+}$, Zr^{4+}, Hf^{4+}, etc.)[12–16], and the lithium thiophosphates such as $Li_{10}GeP_2S_{12}$,[17–21] Li_2S-P_2S_5 glasses,[22–26] the thio-LISICONS,[27–31] and the Li_6PS_5X argyrodites.[32–42] While the thiophosphates are sensitive to ambient atmosphere and may not have the largest potential window, they demonstrate high ionic conductivity and high ductility, improving the processability and resulting contact to the active materials.[17,43,44]

Standing out within this family of materials, the halide-containing argyrodites Li_6PS_5X (X = Cl, Br, I) have been explored with increasing interest. A model crystal structure of the lithium argyrodites, first reported by Deiseroth and coworkers,[33] is shown in Figure 1. The unit cell consists of a face-centered cubic lattice of halide ions (Wyckoff 4a) with PS_4^{3-} tetrahedra occupying the octahedral voids (P sitting on Wyckoff 4b) created by the halide ions. The two possible sites for S are the tetrahedral site (Wyckoff 16e) and the site Wyckoff 4d that is often referred to as the "free sulfur site".[45] Past studies of the lithium substructure within these argyrodites identified the existence of two possible lithium sites, where a transition state (Wyckoff 24g) for short range ion jumps between the main Wyckoff 48h positions exists.[37–39,45] It has been established that the halide ion plays a major role in the ionic transport of the argyrodites: conductivities range from 10^{-6} Scm^{-1} (Li_6PS_5I) to 10^{-3} Scm^{-1} (Li_6PS_5Cl), with Li_6PS_5Br falling in between.[38] This conductivity enhancement is heavily influenced by the appearance of a site-disorder between the free sulfur anion on Wyckoff 4d with the halide on 4a;[37,38] the disorder increases from the iodide (0 %) to the chloride (~60 %).[38]

A variety of different substitution series have already been performed on the argyrodites to probe underlying influences on the conductivity.[32,36–39,45–47] Substitution of the halides to form solid solutions of Cl/Br or Br/I has demonstrated clear effects on alteration of the anion site-disorder, with associated changes in ionic conductivity, but the disorder effects are coupled with compositional differences.[38] Aliovalent substitution has also led to conductivity enhancements in the iodide structures, by substituting P with Si, Ge, and Sn, with large reductions in activation energies; effects in this case are also coupled with increases in Li content.[36,37] Introduction of Se in place of S in Li_6PS_5Br was explored as a method to increase the polarizability of the lattice, but induced competing effects by reduction of the beneficial S^{2-}/Br^- disorder.[46] Li_6PS_5I has the lowest ionic conductivity of the halide argyrodites (also having the lowest anion site disorder), but the capacity to improve its conductivity based on these substitutions justifies more exploration of the composition. While the aliovalent substitution described above has led to ionic conductivities in the range of 10^{-2} S·cm^{-1}, it remains unclear if larger improvements may be possible using isoelectronic substitution, and by what mechanism such improvements would arise.
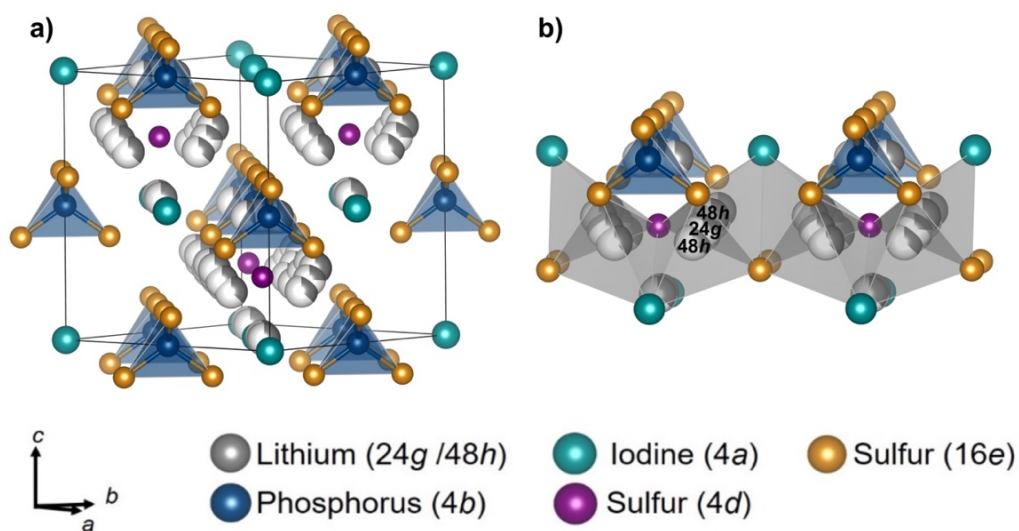

Figure 1. a) Unit cell of Li_6PS_5I. The halide ions construct a face-centered cubic lattice with the free sulfur anion occupying half of the tetrahedral voids. Additionally, the PS_4^{3-} tetrahedra occupy the octahedral voids of the face-centered cubic lattice. b) Lithium forms cluster-like arrangements around the free sulfur site. The Li^+ diffusion pathways are shown in grey.

Often when optimizing the ionic conductivity of solid electrolytes, effort is focused primarily on altering static structural influences such as by modifying the lithium concentration, finding materials with face-sharing polyhedra, and expanding the width of the diffusion pathways and

structural bottlenecks.[3,12,20,48] While this is a very valuable approach, recently the idea of altering the lattice dynamics through introducing softer, more polarizable anions has resurfaced.[7,38,49–51] The idea of softer lattices stems from considerations of transition state theory for ionic conduction,[52,53] and that a softer anion lattice due to altered anion polarizability results in weaker bonds, leading to a larger displacement amplitude for a mobile ion moving through the lattice. This larger displacement amplitude is thought to lead to faster ionic transport by lowering the associated activation barrier.[51,54] This influence of the lattice dynamics on the ionic transport has recently been corroborated using the average vibrational frequency (phonon band center) as well as the Debye frequency as a descriptor for lattice dynamics.[7,38,49–51] Further, recently a coupling of rotational disorder and Li^+ translation has been brought into the discussion in the lithium argyrodites.[55]

Following these ideas of lattice softening and wider diffusion pathways positively influencing ionic conduction, in this work we introduce a series of isoelectronic substitutions within $Li_6PS_{5-x}Se_xI$. Using a combination of structural analysis *via* Rietveld refinements against X-ray diffraction data and impedance spectroscopy to assess ionic transport, we show the influences of selenium substitution in $Li_6PS_{5-x}Se_xI$. Furthermore, by measuring the Raman vibrational spectra and pulse-echo speed of sound to obtain the changing Debye frequencies, the changing lattice dynamics are explored. The substitution of S with Se leads to an increase of the ionic conductivity of up two orders of magnitude from the unsubstituted Li_6PS_5I. This increase in conductivity stems from a linear decrease of the activation barrier that can be explained by the changing static structural features of wider diffusion pathways as well as a softer more polarizable lattice.

2. EXPERIMENTAL METHODS

Synthesis. The preparations for all samples within the $Li_6PS_{5-x}Se_xI$ substitution series were carried out under argon atmosphere. Li_2S (Alfa Aesar, 99.9 %), P_2S_5 (Sigma Aldrich, 99 %) and Se (Alfa Aesar, 99.999 %) were used as received. LiI (Alfa Aesar, 99.95 %) was dried for at least 48 h at 450 °C under dynamic vacuum to remove the majority of $LiI·(H_2O)$ (see Supporting Information Figure S1). Li_2Se was prepared by a gas phase reaction of Se with lithium metal (Alfa Aesar, 99.9 %), using the same approach as recently reported.[49] The chemicals were mixed in their stoichiometric ratio, hand ground in an agate mortar for at least 15 minutes and pressed into dense pellets before loading into ~10 cm long quartz ampoules (10 mm inner diameter) that had each been pre-heated at 800 °C for at least 1.5 hours under dynamic vacuum to ensure the removal of all traces of water. The ampoules containing the powder

mixtures were sealed under vacuum before the reactions were performed at 550 °C for 2 weeks and afterwards air quenched to room temperature. Quenching of the ampoules was needed for a selenium content of x > 3, in order to prevent phase segregation, therefore, all samples were quenched to ensure better comparability.

X-Ray diffraction and structural analysis. X-Ray diffraction experiments were carried out on a STOE Stadi P in Debye-Scherrer geometry. The diffractometer is equipped with two DECTRIS MYTHEN detectors and a silver anode (λ = 0.5594 Å, Ge(111) monochromator) Rietveld refinements were carried out using the TOPAS software package.[56] A visual assessment, as well as the fit indicator goodness-of-fit (GOF) were used to determine the quality of the fits. A Chebyshev function of 10 parameters was used to fit the background. For the peak shape modelling a modified Thomson-Cox-Hastings pseudo-Voigt function was employed. The used constraints can be found in the structural tables in the Supporting Information.

Electrochemical impedance spectroscopy. Electrical conductivities were measured using AC impedance spectroscopy, using pellets with a thickness of ~2 mm and a geometric density of >85 % packed into argon filled pouch cells. The pellets were isostatically pressed and afterwards annealed for 15 minutes at 550 °C. Evaporated gold electrodes (0.53 cm^2) were used for contacting. The electrochemical impedance analysis (EIS) was conducted in the temperature range of -40 °C to 60 °C using a VMP300 impedance analyzer (Biologic) at a frequency range of 7 MHz to 100 mHz with an amplitude of 10 mV. In order to obtain statistical information, three pellets of each composition were prepared and measured separately.

Speed of sound measurements. Pulse-echo speed of sound measurements were performed on consolidated discs using an Epoch 600 (Olympus) with 5 MHz transducers for longitudinal and transverse speeds of sound. The samples were coated with a thin layer (< 200 nm) of gold in order to prevent side reactions of the sample with the couplant honey. All measurements were performed under nitrogen atmosphere. Three pellets of each composition were measured, with at least two responses per pellet, and these three data sets used to determine the average speeds of sound, thereby reducing the measurement uncertainty.

Raman spectroscopy. The samples were placed on a microscopy glass slide and sealed air-tight with grease and a glass coverslip. A Senterra Raman spectrometer (Bruker Optics) was used with an excitation wavelength of 532 nm. A resolution of 3-5 cm^{-1} was achieved in the

range of 47-1548 cm^{-1} with a 20x magnification lens using an integration time of 3 s per spectrum and 100 spectra per measurement. A low laser power of 0.2 mW was used to prevent sample decomposition.

3. RESULTS AND DISCUSSSION

Structural changes. The solid solutions of Li$_6$PS$_{5-x}$Se$_x$I were chosen in order to observe lattice effects independent of any halide anion site-disorder (due to the negligible disorder present in the I argyrodites),[37,38,46] as this would further complicate the structure-transport analysis, with the benefit that the compositions studied are distinguishable due to differences in X-ray scattering form factors of S, Se and I.
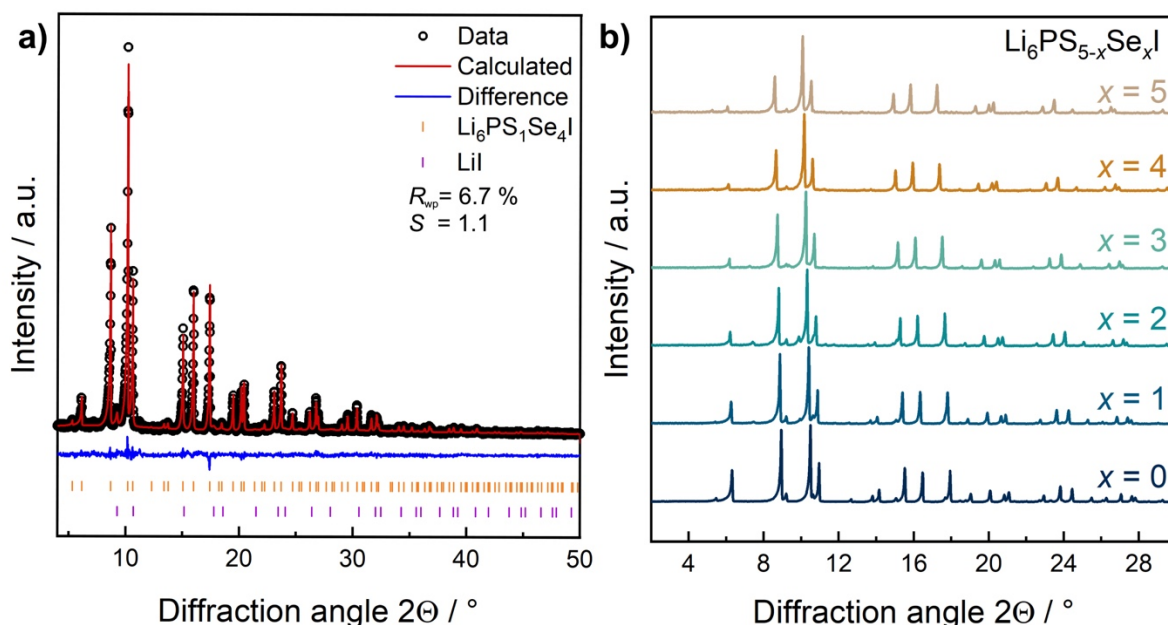

Figure 2. a) Rietveld-refinement example of Li$_6$PS$_1$Se$_4$I including the LiI impurity phase (~3.5 wt.%) and b) all obtained diffraction patterns of the solid solutions Li$_6$PS$_{5-x}$Se$_x$I.

In order to study the structural changes within the Li$_6$PS$_{5-x}$Se$_x$I solid solution series, compositions with a step size of x = 1 of increasing selenium content were synthesized by classical methods and investigated using Rietveld refinements against X-ray diffraction data. Figure 2 shows a representative Rietveld refinement for the composition of Li$_6$PS$_1$Se$_4$I and all X-ray diffraction patterns for comparison. All other refinement results can be found in the Supporting Information (Figures S2 – S7). While a minor contribution of LiI can be found as an impurity phase, a linear expansion of the lattice parameters caused by the larger ionic radius of selenium (198 pm) in comparison to sulfur (184 pm)[57] can be observed, thus obeying

Vegard's rule[58] (Figure 3a). The absence of a major selenium rich impurity phase indicates a true solid solution for the $Li_6PS_{5-x}Se_xI$ system without the existence of a solubility limit. Small impurity fractions of $LiI(H_2O)$ can still be found for the solid solutions of $x < 3$, which seem to only occur when Li_2S is used as a precursor. Additional structural features such as the Se occupancy on the free chalcogenide site (Wyckoff $4d$), the Se occupancy on the $PS_{4-x}Se_x{}^{3-}$ tetrahedra (Wyckoff $16e$) and the volume of the $P(S/Se)_4{}^{3-}$ tetrahedra can be found in Figure 3 as well. Similar to the lattice parameters, the incorporation of selenium leads to an expansion of the $P(S/Se)_4{}^{3-}$ tetrahedra. With increasing degree of substitution, the amount of sulfur and selenium on the free sulfur site as well as on the $P(S/Se)_4{}^{3-}$ tetrahedra increases (Figure 3c and 3d). The overall change in the Se occupancy on both lattice sites suggests an even distribution between the sites and no clear site preference for Se. While unsubstituted Li_6PS_5I exhibits no significant site-disorder between I^- and S^{2-}, a minor change in the disorder can be found during Se substitution, to a maximum of $\sim$ 7 % (see Supporting Information Figure S8).[38]
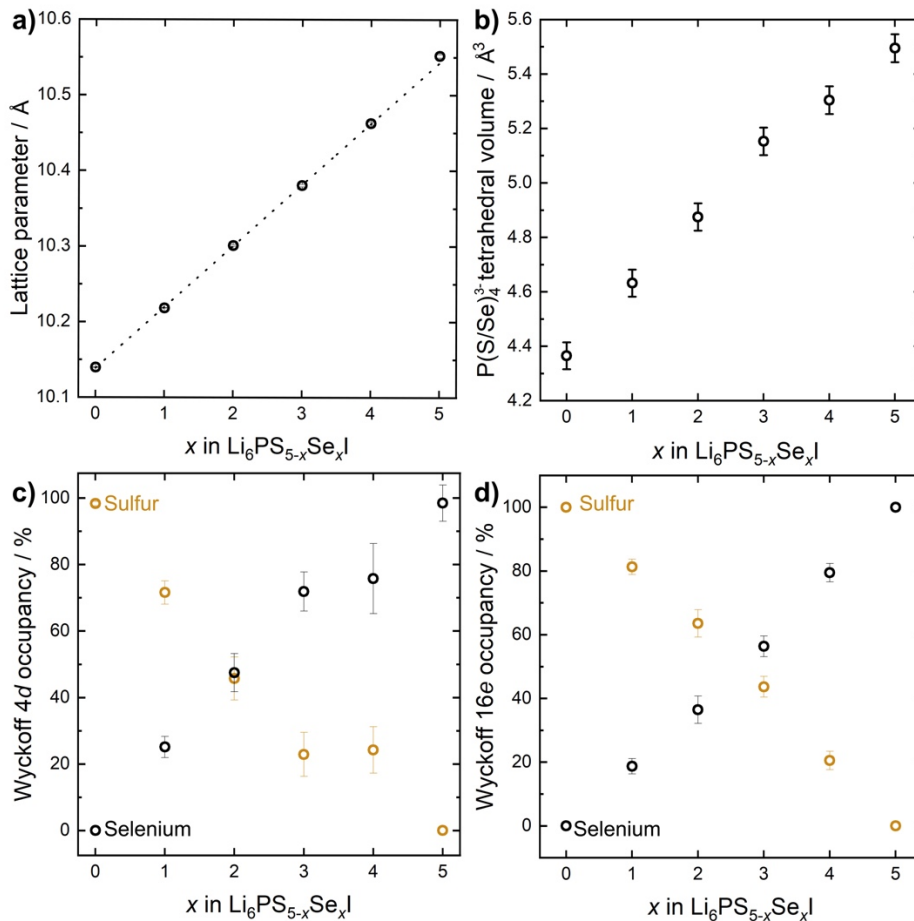

Figure 3. a) The incorporation of the larger selenium leads to an expansion of the unit cell, as well as the b) $P(S/Se)_4{}^{3-}$ tetrahedral volume. A true solid solution is indicated by the linear expansion of the lattice, indicating the absence of a solubility limit for selenium within Li_6PS_5-
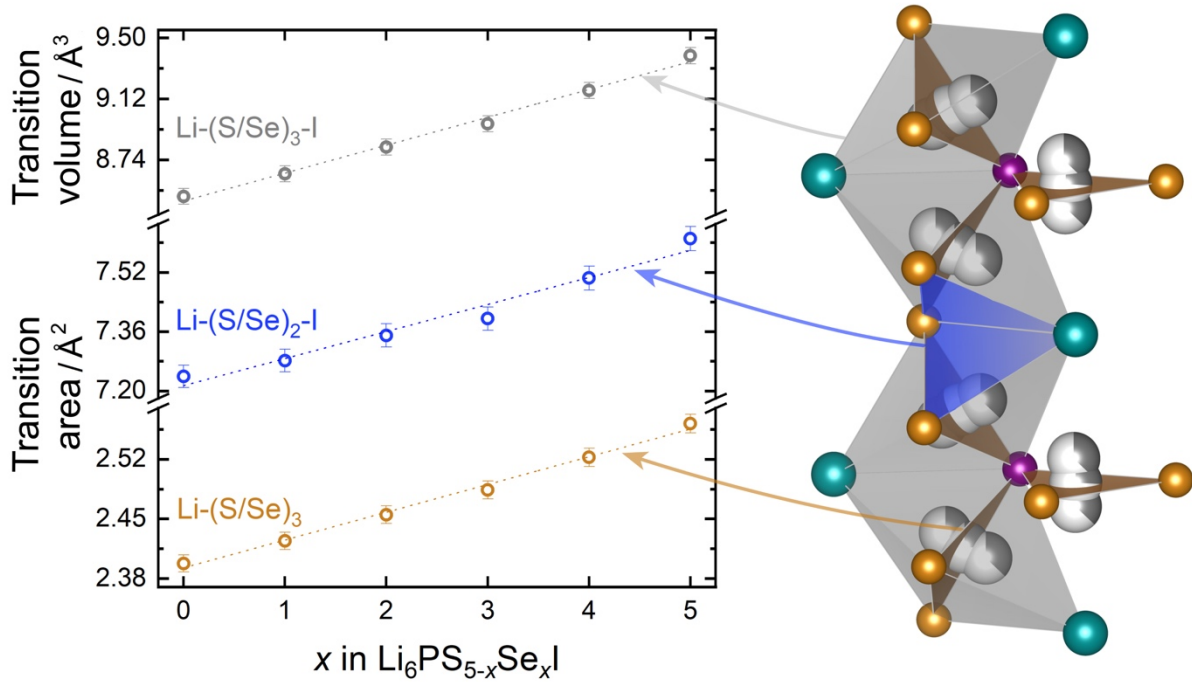
Figure 4. A steadily increasing selenium occupancy and expanding lattice leads to wider diffusion pathways for Li$^+$. Shown are the resulting Li$^+$ coordination-tetrahedra (Li-(S/Se)$_3$-I) in grey, the long-range inter-cage jump transition area (Li-(S/Se)$_2$I) (blue) and the short-range intra-cage jump transition area (Li(S/Se)$_3$) (orange).

The expansion of the P(S/Se)$_4$$^{3-}$ tetrahedra is in close structural vicinity to Li$^+$ and hence an influence on the diffusion pathways can be expected. Two different Li$^+$ positions are known in Li$_6$PS$_5$X, namely the Wyckoff 48*h* and 24*g*, which form cages around the free S^{2-} in the tetrahedral voids of the face-centered cubic lattice.[33,45] These two positions give rise to three different jump processes: (i) a so-called doublet jump from 48*h* via 24*g* to another 48*h* position, (ii) an intra cage-jump of 48*h* to 48*h*, and (iii) an inter-cage jump from position 48*h* to 48*h*. While the inter-cage jumps seem to be the rate-limiting step for the Li$^+$ jump process and overall measurable ionic conductivity,[37,38,45,59] the structural features around all jumps are of interest as they directly influence the diffusion behavior for lithium.

Figure 4 shows the evolution of the Li-(S/Se)$_3$ triangular transition area and the corresponding Li-(S/Se)$_3$I tetrahedra with increasing Se content, both of which describe the pathways of the doublet jump and intra-cage jump. Further shown is the side of a Li-(S/Se)$_3$I tetrahedron, coordinated by I, (S/Se) and (S/Se). This side of the tetrahedron is the bottleneck for the inter-

cage jump as the lithium ions will have to pass through this triangle during the jump from one cage to another. While the X-ray diffraction data makes it impossible to locate the Li^+ in the structure, Figure 3 shows that all anionic structural features describing the diffusion pathways widen geometrically, which will likely affect the overall ionic transport.

Lattice dynamics. Recently, there has been increased interest in understanding the influence of the lattice vibrations and dynamics on the ionic transport in ionic conductors.[38,50,60] With the incorporation of a more polarizable anion, the lattice vibrational properties were observed to soften, which in turn affects the ionic transport by decreasing the enthalpy and entropy of migration.[38,49–51] Further, it was recently shown that additional polyhedral anion dynamics exist that are coupled to the Li^+ translation.[55] However, in the Li_6PS_5I series reported here, the Li^+ ion jumps and rotational dynamics are independent of each other, which beneficially prevents further complication of the analysis. In this work, the resulting lattice dynamics are assessed using the optical and acoustic modes of the dispersion relation.[61,62] Raman spectroscopy and the measurement of the speed of sound within a material can give reliable information regarding the phonon dynamics and average phonon frequencies.[38,49,50,63–65]

Figure 5a shows the influence of increasing selenium occupancy on the stretching mode of the $PS_{4-y}Se_y^{3-}$ tetrahedra. First, the appearance of multiple, isolated $PS_{4-y}Se_y^{3-}$ tetrahedral species can be observed for the mixed S/Se compounds that correspond to a symmetry reduction from T_d to C_{3v} and eventually C_{2v} with increasing degree of substitution. Such a behavior has already been reported for the $Na_3PS_{4-x}Se_x$ system by Krauskopf *et al.*[50], who also showed that a binomial distribution well describes the occurrence of such mixed tetrahedra. This interchangeability of sulfur and selenium on the tetrahedral sites suggests similar formation energies for ordered and partially disordered tetrahedra even for different types of compounds. Figure 5b shows the correlation between the average crystallographic bond length (and therefore bond strength) and the corresponding Raman shift. With increasing Se content and increasing bond length, the Raman shift decreases. The PSe_4^{3-} tetrahedra show an increasing Raman shift at higher Se content which trends counter to the overall observed changes, suggesting some additional underlying local processes. Overall, the decreasing Raman shift with respect to the change of the average bond length indicates a softening of the optical phonons when substituting S for Se in $Li_6PS_{5-x}Se_xI$, similar to the one recently found for $Na_3PS_{4-x}Se_x$.[50]
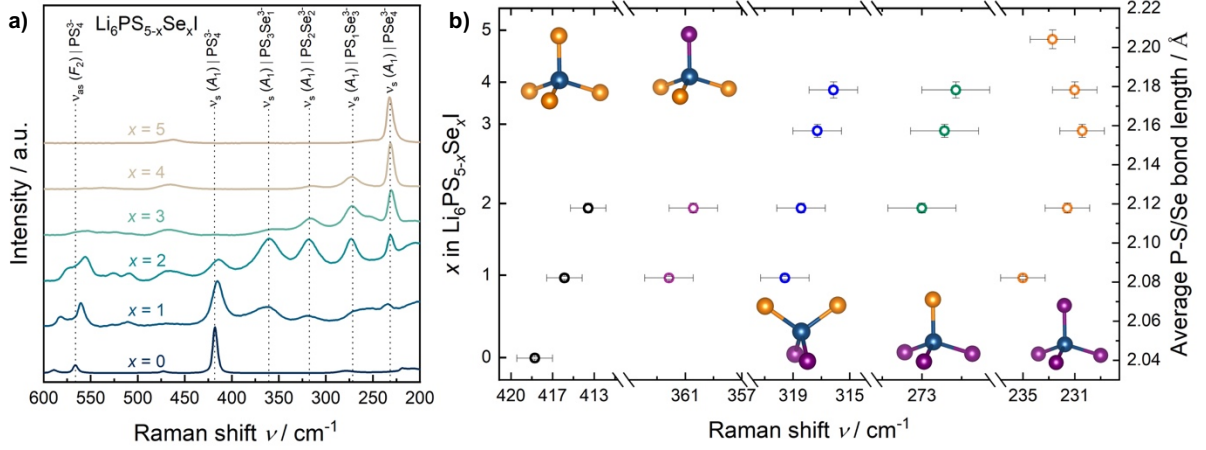
Figure 5. a) Obtained Raman spectra showing the formation of new, isolated PS$_{4-y}$Se$_y$ tetrahedra. b) The vibrational energy reduction within the different PS$_{4-y}$Se$_y$ tetrahedra with respect to the average bond length indicates a softening of the optical vibrational modes.

As the Raman measurements only give insight into the optical phonons, the acoustic phonons were assessed using speed of sound measurements. Measuring the longitudinal and transverse speeds of sound probes the group velocity of lattice oscillations close to the center of the Brillouin zone, which can be expressed as the slope of the dispersion relation in this region (see inset Figure 6b).[50] Using a calculated mean speed of sound v_m and average volume per atom V, the Debye frequency v_D can be obtained and it can be used as a descriptor of the average lattice dynamics.[50,65]

$$v_D = \left(\frac{3}{4\pi V}\right)^{\frac{1}{3}} v_m \quad , with \ v_m = \left(\frac{3}{v_{long}^{-3} + 2v_{trans}^{-3}}\right)^{\frac{1}{3}} \qquad \text{Eq. (1)}$$

Figure 6 shows the different speeds of sound and the resulting Debye frequencies of the lattices of these solid solutions. As expected, with increasing selenium content in Li$_6$PS$_{5-x}$Se$_x$I the speed of sound and Debye frequencies decrease, indicating an overall softening of the lattice. In other words, the larger and more polarizable Se anion leads to a decrease in the energy of the lattice vibrations and softer/weaker bonding in the framework.
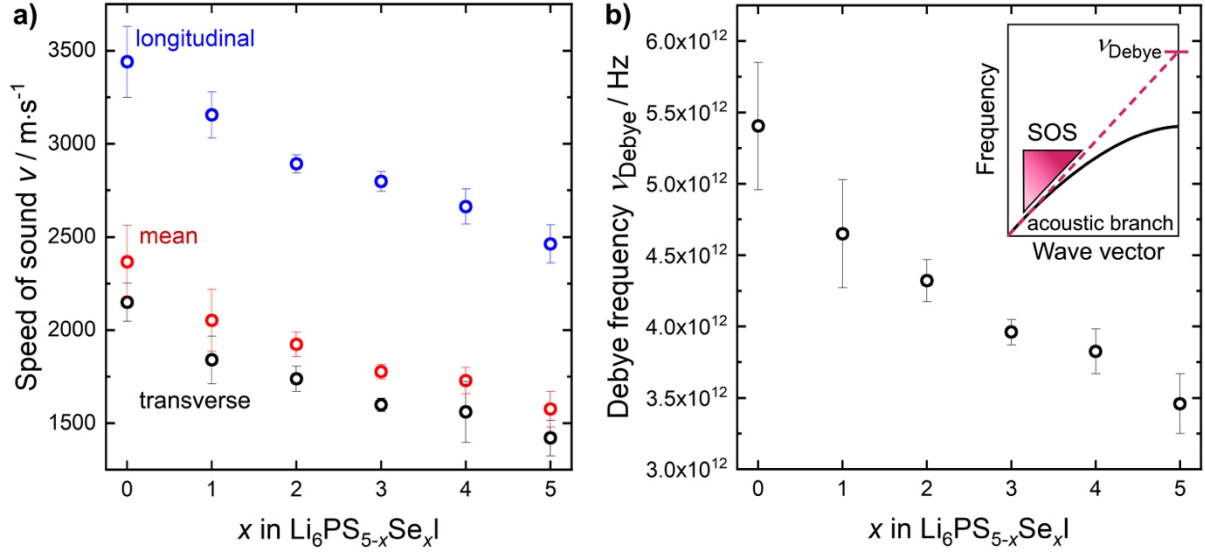
Figure 6. a) Observed speeds of sound and b) Debye frequencies indicate a softening of the acoustic phonons with increasing Se content in Li₆PS₅₋ₓSeₓI. Error bars correspond to standard deviations obtained from measurements on three samples per composition. The inset shows a schematic relation of the Debye frequency to the speed of sound within a phonon dispersion curve.

Ionic transport. The ionic transport properties of the $Li_6PS_{5-x}Se_xI$ series were assessed using temperature-dependent impedance spectroscopy. Representative room-temperature Nyquist-plots, as well as the resulting Arrhenius plots, are shown in Figure 7. Small grain boundary contributions and an electrode roughness can be seen that lead to a slight asymmetry for the low frequency region of the semicircle. The conductivities shown here represent the bulk contribution of ionic transport as all processes can be distinguished based on the process capacitances.[66–68] For instance in Li_6PSe_5I, the bulk contributions show capacitances in the range of 59 pF·cm⁻² and the grain boundary/electrode roughness contributions in the range of 34 nF·cm⁻². Further, alpha factors of up to 0.96 for the bulk contribution indicate the ideality of the process.[69]

Figure 7 shows the obtained Nyquist plots of all compositions, normalized to the pellet thickness for comparison. The employed equivalent circuit is shown in the inset. The activation barriers for ionic migration and the corresponding conductivities, both extracted from the Arrhenius plots, can also be found. A significant, linear decrease of the activation barrier can be observed with increasing Se content. This decrease of the activation barrier is governed by an increase of ionic conductivity of up to 2 orders of magnitude leading to an ionic conductivity of 0.28 mS·cm⁻¹ compared to 0.0025 mS·cm⁻¹ for the unsubstituted Li_6PS_5I.

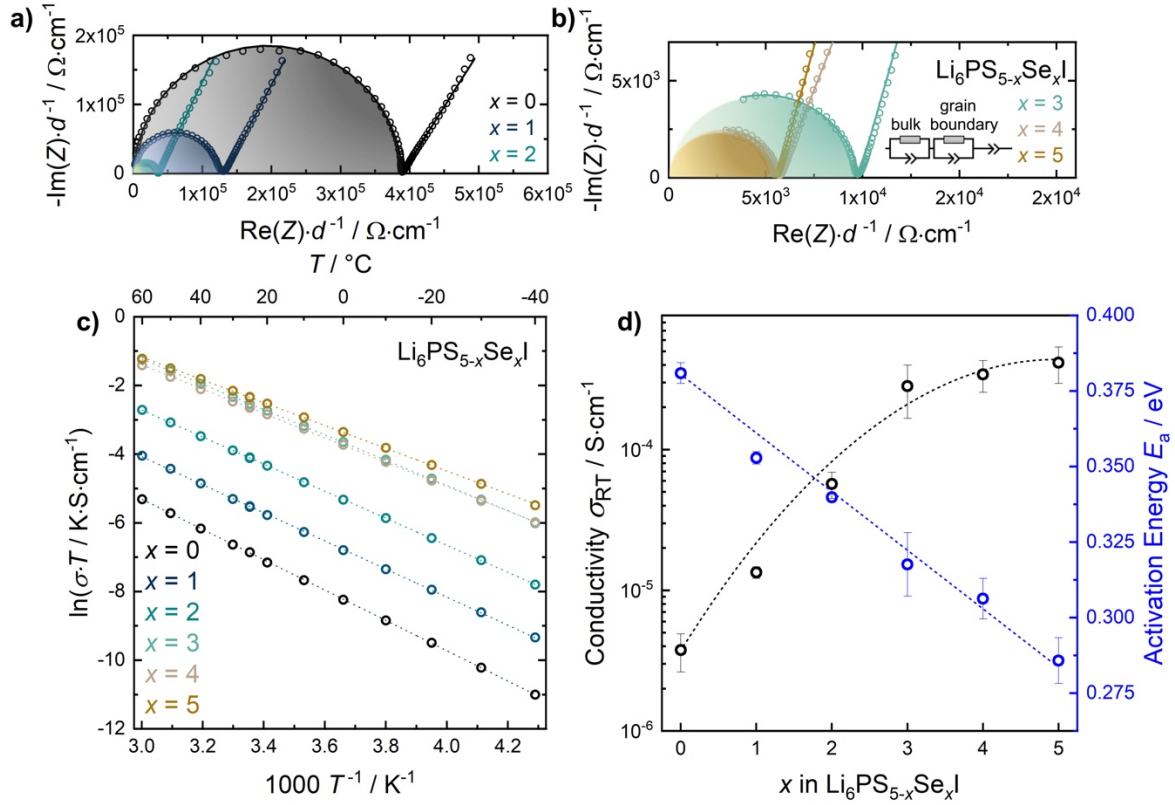*Figure 7: a) and b) Impedance spectra of all compositions of $Li_6PS_{5-x}Se_xI$ at room temperature, showing the ideality of the measurements and the equivalent circuit that was used for fitting. c) Calculated Arrhenius diagrams showing the good fit quality and d) room-temperature conductivity and activation barriers. The Se substitution leads to a decreasing activation barrier and results in an increased conductivity over multiple orders of magnitude. Error bars correspond to standard deviations obtained from measurements on three samples per composition.*

Structure - property relationships. Figure 8 shows the influence of the expanding lithium transition polyhedra on the measured activation barrier as well as the correlation to the lattice dynamics. Using the three different structural descriptors for the diffusion pathway introduced above, *i.e.* (i) the triangular transition areas for the short range doublet jump and (ii) the long range intercage jump as well as the (iii) resulting $Li(S/Se)_3I$ tetrahedral volume, a clear correlation can be found. With increasing width of the diffusion pathways that govern the jumps within the Li^+ cage and from cage to cage (inter-cage jump), the activation barrier decreases (Figure 8a). As lithium jumps between adjacent sites, the ions surrounding the diffusion pathway have to be displaced. This is often referred to as the bottleneck for diffusion. By

increasing the static structure, and with it the size of this bottleneck, the required energetic barrier for the ionic jump is reduced.

In addition to the width of the diffusion pathways, the overall softness and polarizability of the lattice also plays a role (Figure 8b). With increasing selenium content, the lattice softens and less energy needs to be expended displacing the lattice during the jump. This influence of an increasing lattice polarizability leading to a reduced activation barrier has recently been shown in a variety of Li^+ and Na^+ superionic conductors.[38,49,50] In this work, the minor disorder induced on the anion site (Figure S8) does not seem to correlate to the boost in conductivity, suggesting the lattice softening and diffusion pathway widening as a primary mechanism for better ionic transport. This is in contrast to work on Li_6PS_5Br, where Se subsitution induced a substantial decrease in anion site disorder, convoluting the effects on conductivity.[46]

Overall, $Li_6PS_{5-x}Se_xI$ clearly represents an example in which lattice softening coupled with diffusion pathway widening strongly influences ionic transport, and shows great promise if it can be engineered without affecting beneficial anion disorder in the other argyrodites.
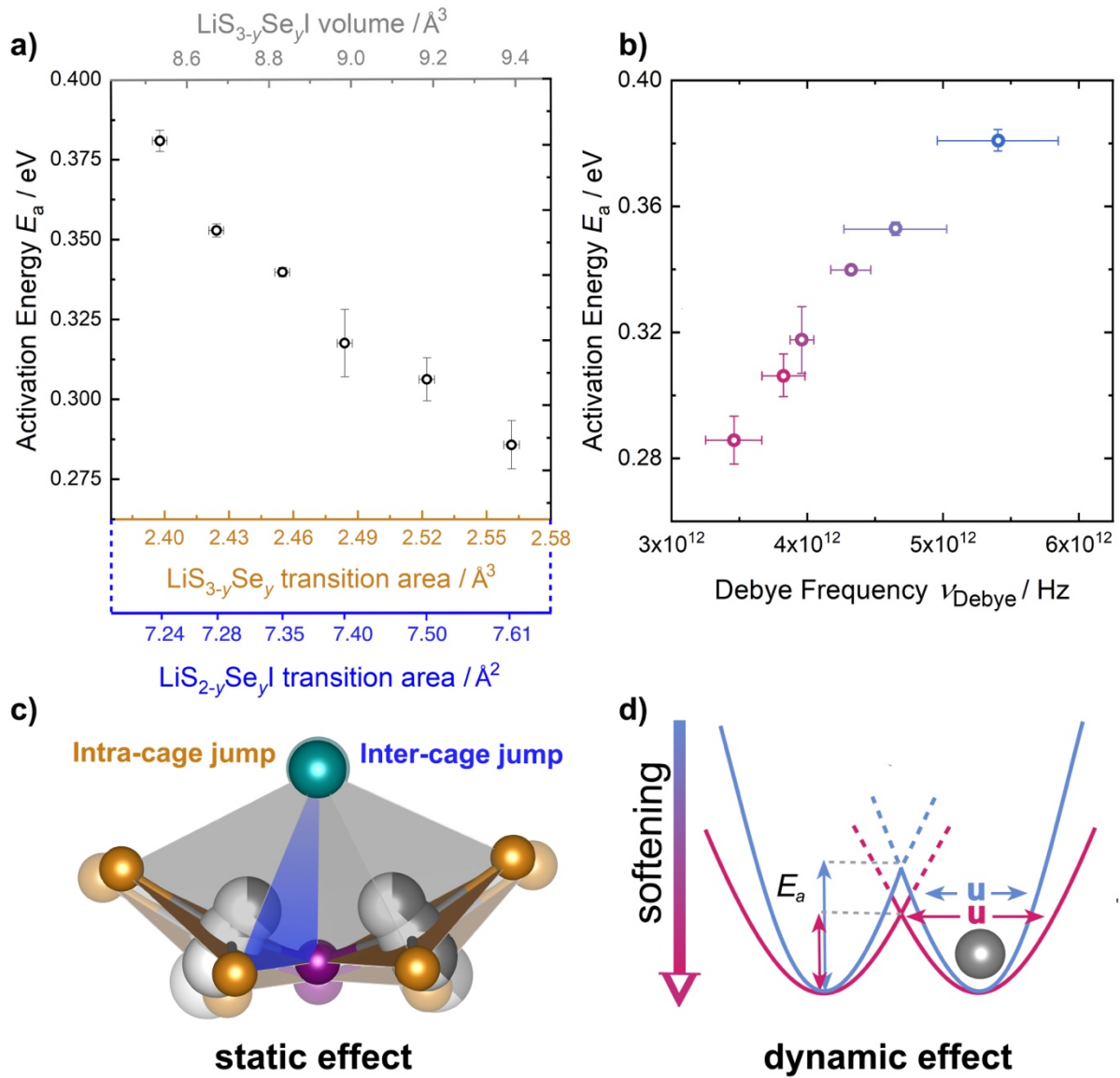
Figure 8. a) Structure property relationship between the activation barrier and the transition area for Lithium diffusion. The decreasing activation barrier is attributed to a simplified transition with increasing area size. b) Furthermore, a direct correlation between the lattice dynamics and the activation barrier is shown. The Debye frequency shows a linear relation to the activation barrier. c) Schematic on the diffusion pathways and influence of wider bottlenecks, related to the data in a). d) Schematic of the effect of lattice softening on the ionic jump. The changing Debye frequency and softer lattice leads to wider oscillator potentials and lower barriers, related to the data in (b).

4. CONCLUSION

In this work, we report the successful incorporation of Se into the argyrodite structure leading to the substitution series of $Li_6PS_{5-x}Se_xI$. The linear lattice expansion and absence of a selenium rich impurity phase indicate the formation of true solid solutions. The incorporation of the larger and more polarizable anion results in a decrease in the observable activation barrier for ionic migration, resulting in a conductivity increase of around 2 orders of magnitude. The decreasing activation barrier can be directly related to changes in the static lattice structure and its lattice dynamics, showing that wider diffusion pathways and more polarizable lattices can positively influence ionic conduction in the argyrodite superionic conductors. Moreover, given that the conductivity of the iodide argyrodite was drastically increased without the influence of increased anion site disorder (which has been suggested to play a major role in the series of the halide argyrodites), this work highlights the effects of lattice softening that could be exploited for improving other known compositions.

Supporting Information.

The effect of pre-drying of the LiI precursor is shown. In addition, all structural data as obtained from Rietveld refinements can be found here.

AUTHOR INFORMATION

Corresponding Authors

*wolfgang.g.zeier@pc.jlug.de;

Notes

The authors declare no competing financial interests.

References

(1)   Kato, Y.; Hori, S.; Saito, T.; Suzuki, K.; Hirayama, M.; Mitsui, A.; Yonemura, M.; Iba, H.; Kanno, R. High-Power All-Solid-State Batteries Using Sulfide Superionic Conductors. *Nat. Energy* **2016**, *1*, 16030.

(2)   Janek, J.; Zeier, W. G. A Solid Future for Battery Development. *Nat. Energy* **2016**, *1*,pp. 16141.

(3)   Culver, S. P.; Koerver, R.; Krauskopf, T.; Zeier, W. G. Designing Ionic Conductors: The Interplay between Structural Phenomena and Interfaces in Thiophosphate-Based Solid-State Batteries. *Chem. Mater.* **2018**, *30*, 4179–4192.

(4)   Ghidiu, M.; Ruhl, J.; Culver, S. P.; Zeier, W. G. Solution-Based Synthesis of Lithium Thiophosphate Superionic Conductors for Solid-State Batteries: A Chemistry Perspective. *J. Mater. Chem. A* **2019**, *7*, 17735–17753.

(5)   Kato, Y.; Shiotani, S.; Morita, K.; Suzuki, K.; Hirayama, M.; Kanno, R. All-Solid-State Batteries with Thick Electrode Configurations. *J. Phys. Chem. Lett.* **2018**, *9*, 607–613.

(6)   Asano, T.; Sakai, A.; Ouchi, S.; Sakaida, M.; Miyazaki, A.; Hasegawa, S. Solid Halide Electrolytes with High Lithium-Ion Conductivity for Application in 4 V Class Bulk-Type All-Solid-State Batteries. *Adv. Mater.* **2018**, *30*, 1803075.

(7)   Muy, S.; Voss, J.; Schlem, R.; Koerver, R.; Sedlmaier, S. J.; Maglia, F.; Lamp, P.; Zeier, W. G.; Shao-Horn, Y. High-Throughput Screening of Solid-State Li-Ion Conductors Using Lattice-Dynamics Descriptors. *iScience* **2019**, *16*, 270–282.

(8)   Cussen, E. J. Structure and Ionic Conductivity in Lithium Garnets. *J. Mater. Chem.* **2010**, *20*, 5167–5173.

(9)   Li, Y.; Han, J. T.; Wang, C. A.; Vogel, S. C.; Xie, H.; Xu, M.; Goodenough, J. B. Ionic Distribution and Conductivity in Lithium Garnet $Li_7La_3Zr_2O_{12}$. *J. Power Sources* **2012**, *209*, 278–281.

(10)   Rettenwander, D.; Redhammer, G.; Preishuber-Pflügl, F.; Cheng, L.; Miara, L.; Wagner, R.; Welzl, A.; Suard, E.; Doeff, M. M.; Wilkening, M.; Fleig, J.; Amthauer, G. Structural and Electrochemical Consequences of Al and Ga Cosubstitution in $Li_7La_3Zr_2O_{12}$ Solid Electrolytes. *Chem. Mater.* **2016**, *28*, 2384–2392.

(11)   Murugan, R.; Thangadurai, V.; Weppner, W. Fast Lithium Ion Conduction in Garnet-Type $Li_7La_3Zr_2O_{12}$. *Angew. Chemie - Int. Ed.* **2007**, *46*, 7778–7781.

(12)   Guin, M.; Tietz, F.; Guillon, O. New Promising NASICON Material as Solid Electrolyte

for Sodium-Ion Batteries: Correlation between Composition, Crystal Structure and Ionic Conductivity of $Na_{3+x}Sc_2Si_xP_{3-x}O_{12}$. *Solid State Ionics* **2016**, *293*, 18–26.

(13)   Guin, M.; Tietz, F. Survey of the Transport Properties of Sodium Superionic Conductor Materials for Use in Sodium Batteries. *J. Power Sources* **2015**, *273*, 1056–1064.

(14)   Arbi, K.; Rojo, J. M.; Sanz, J. Lithium Mobility in Titanium Based Nasicon $Li_{1+x}Ti_{2-x}Al_x(PO_4)_3$ and $LiTi_{2-x}Zr_x(PO_4)_3$ Materials Followed by NMR and Impedance Spectroscopy. *J. Eur. Ceram. Soc.* **2007**, *27*, 4215–4218.

(15)   El-Shinawi, H.; Greaves, C.; Janek, J. Sol-Gel Synthesis and Room-Temperature Properties of α-$LiZr_2(PO_4)_3$. *RSC Adv.* **2015**, *5*, 17054–17059.

(16)   Breuer, S.; Prutsch, D.; Ma, Q.; Epp, V.; Preishuber-Pflügl, F.; Tietz, F.; Wilkening, M. Separating Bulk from Grain Boundary Li Ion Conductivity in the Sol-Gel Prepared Solid Electrolyte $Li_{1.5}Al_{0.5}Ti_{1.5}(PO_4)_3$. *J. Mater. Chem. A* **2015**, *3*, 21343–21350.

(17)   Kamaya, N.; Homma, K.; Yamakawa, Y.; Hirayama, M.; Kanno, R.; Yonemura, M.; Kamiyama, T.; Kato, Y.; Hama, S.; Kawamoto, K.; Mitsui, A. A Lithium Superionic Conductor. *Nat. Mater.* **2011**, *10*, 682–686.

(18)   Weber, D. A.; Senyshyn, A.; Weldert, K. S.; Wenzel, S.; Zhang, W.; Kaiser, R.; Berendts, S.; Janek, J.; Zeier, W. G. Structural Insights and 3D Diffusion Pathways within the Lithium Superionic Conductor $Li_{10}GeP_2S_{12}$. *Chem. Mater.* **2016**, *28*, 5905–5915.

(19)   Kuhn, A.; Gerbig, O.; Zhu, C.; Falkenberg, F.; Maier, J.; Lotsch, B. V. A New Ultrafast Superionic Li-Conductor: Ion Dynamics in $Li_{11}Si_2PS_{12}$ and Comparison with Other Tetragonal LGPS-Type Electrolytes. *Phys. Chem. Chem. Phys.* **2014**, *16*, 14669–14674.

(20)   Krauskopf, T.; Culver, S. P.; Zeier, W. G. Bottleneck of Diffusion and Inductive Effects in $Li_{10}Ge_{1-x}Sn_xP_2S_{12}$. *Chem. Mater.* **2018**, *30*, 1791–1798.

(21)   Harm, S.; Hatz, A. K.; Moudrakovski, I.; Eger, R.; Kuhn, A.; Hoch, C.; Lotsch, B. V. Lesson Learned from NMR: Characterization and Ionic Conductivity of LGPS-like Li_7SiPS_8. *Chem. Mater.* **2019**, *31*, 1280–1288.

(22)   Dietrich, C.; Weber, D. A.; Sedlmaier, S. J.; Indris, S.; Culver, S. P.; Walter, D.; Janek, J.; Zeier, W. G. Lithium Ion Conductivity in Li_2S-P_2S_5 Glasses-Building Units and Local Structure Evolution during the Crystallization of Superionic Conductors Li_3PS_4, $Li_7P_3S_{11}$ and $Li_4P_2S_7$. *J. Mater. Chem. A* **2017**, *5*, 18111–18119.

(23)   Tatsumisago, M.; Hama, S.; Hayashi, A.; Morimoto, H.; Minami, T. New Lithium Ion Conducting Glass-Ceramics Prepared from Mechanochemical Li_2S-P_2S_5 Glasses. *Solid State Ionics* **2002**, *154*, 635–640.

(24)   Hayashi, A.; Hama, S.; Morimoto, H.; Tatsumisago, M.; Minami, T. Preparation of Li_2S-P_2S_5 Amorphous Solid Electrolytes by Mechanical Milling. *J. Am. Ceram. Soc.* **2004**, *84*, 477–479.

(25)   Hayashi, A.; Hama, S.; Minami, T.; Tatsumisago, M. Formation of Superionic Crystals from Mechanically Milled Li_2S-P_2S_5 Glasses. *Electrochem. commun.* **2003**, *5*, 111–114.

(26)   Seino, Y.; Ota, T.; Takada, K.; Hayashi, A.; Tatsumisago, M. A Sulphide Lithium Super Ion Conductor Is Superior to Liquid Ion Conductors for Use in Rechargeable Batteries. *Energy Environ. Sci.* **2014**, *7*, 627–631.

(27)   Kanno, R.; Murayama, M. Lithium Ionic Conductor Thio-LISICON: The Li_2S-GeS_2-P_2S_5 System. *J. Electrochem. Soc.* **2001**, *148*, 742–746.

(28)   Kanno, R.; Hata, T.; Kawamoto, Y.; Irie, M. Synthesis of a New Lithium Ionic Conductor, Thio-LISICON-Lithium Germanium Sulfide System. *Solid State Ionics* **2000**, *130*, 97–104.

(29)   Minafra, N.; Culver, S. P.; Li, C.; Senyshyn, A.; Zeier, W. G. Influence of the Lithium Substructure on the Diffusion Pathways and Transport Properties of the Thio-LISICON $Li_4Ge_{1-x}Sn_xS_4$. *Chem. Mater.* **2019**, *31*, 3794–3802.

(30)   Leube, B. T.; Inglis, K. K.; Carrington, E. J.; Sharp, P. M.; Shin, J. F.; Neale, A. R.; Manning, T. D.; Pitcher, M. J.; Hardwick, L. J.; Dyer, M. S.; Blanc, F.; Claridge, J. B.; Rosseinsky, M. J. Lithium Transport in $Li_{4.4}M_{0.4}M'_{0.6}S_4$ (M = Al^{3+}, Ga^{3+}, and M′ = Ge^{4+}, Sn^{4+}): Combined Crystallographic, Conductivity, Solid State NMR, and Computational Studies. *Chem. Mater.* **2018**, *30*, 7183–7200.

(31)   Zhou, L.; Assoud, A.; Shyamsunder, A.; Zhang, Q.; Hartmann, P.; Kulisch, J.; Nazar, L. F. An Entropically Stabilized Fast-Ion Conductor : $Li_{3.25}[Si_{0.25}P_{0.75}]S_4$, *Chem. Mater.* **2019**. https://doi.org/10.1021/acs.chemmater.9b00657.

(32)   Adeli, P.; Bazak, J. D.; Park, K. H.; Kochetkov, I.; Huq, A.; Goward, G. R.; Nazar, L. F. Boosting Solid-State Diffusivity and Conductivity in Lithium Superionic Argyrodites by Halide Substitution. *Angew. Chemie - Int. Ed.* **2019**, *58*, 8681–8686.

(33)   Deiseroth, H. J.; Kong, S. T.; Eckert, H.; Vannahme, J.; Reiner, C.; Zaiß, T.; Schlosser, M. Li_6PS_5X: A Class of Crystalline Li-Rich Solids with an Unusually High Li^+ Mobility. *Angew. Chemie - Int. Ed.* **2008**, *47*, 755–758.

(34)   Rayavarapu, P. R.; Sharma, N.; Peterson, V. K.; Adams, S. Variation in Structure and Li^+-Ion Migration in Argyrodite-Type Li_6PS_5X (X = Cl, Br, I) Solid Electrolytes. *J. Solid State Electrochem.* **2012**, *16*, 1807–1813.

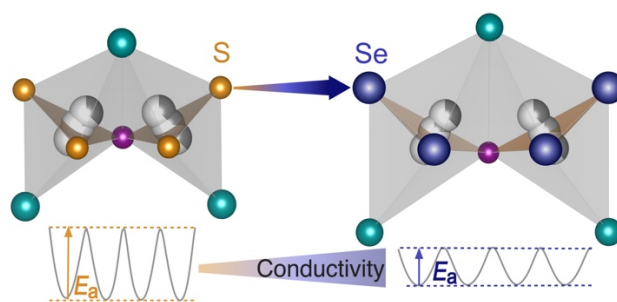(35)   Hanghofer, I.; Brinek, M.; Eisbacher, S. L.; Bitschnau, B.; Volck, M.; Hennige, V.;

Hanzu, I.; Rettenwander, D.; Wilkening, H. M. R. Substitutional Disorder: Structure and Ion Dynamics of the Argyrodites Li_6PS_5Cl, Li_6PS_5Br and Li_6PS_5I. *Phys. Chem. Chem. Phys.* **2019**, *21*, 8489–8507.

(36) Ohno, S.; Helm, B.; Fuchs, T.; Dewald, G.; Kraft, M. A.; Culver, S. P.; Senyshyn, A.; Zeier, W. G. Further Evidence for Energy Landscape Flattening in the Superionic Argyrodites $Li_{6+x}P_{1–x}M_xS_5I$ (M = Si, Ge, Sn) . *Chem. Mater.* **2019**, *31*, 4936–4944.

(37) Kraft, M. A.; Ohno, S.; Zinkevich, T.; Koerver, R.; Culver, S. P.; Fuchs, T.; Senyshyn, A.; Indris, S.; Morgan, B. J.; Zeier, W. G. Inducing High Ionic Conductivity in the Lithium Superionic Argyrodites $Li_{6+x}P_{1-x}Ge_xS_5I$ for All-Solid-State Batteries. *J. Am. Chem. Soc.* **2018**, *140*, 16330–16339.

(38) Kraft, M. A.; Culver, S. P.; Calderon, M.; Böcher, F.; Krauskopf, T.; Senyshyn, A.; Dietrich, C.; Zevalkink, A.; Janek, J.; Zeier, W. G. Influence of Lattice Polarizability on the Ionic Conductivity in the Lithium Superionic Argyrodites Li_6PS_5X (X = Cl, Br, I). *J. Am. Chem. Soc.* **2017**, *139*, 10909–10918.

(39) Minafra, N.; Culver, S. P.; Krauskopf, T.; Senyshyn, A.; Zeier, W. G. Effect of Si Substitution on the Structural and Transport Properties of Superionic Li-Argyrodites. *J. Mater. Chem. A* **2018**, *6*, 645–651.

(40) Yubuchi, S.; Uematsu, M.; Deguchi, M.; Hayashi, A.; Tatsumisago, M. Lithium-Ion-Conducting Argyrodite-Type Li_6PS_5X (X = Cl, Br, I) Solid Electrolytes Prepared by a Liquid-Phase Technique Using Ethanol as a Solvent. *ACS Appl. Energy Mater.* **2018**, *1*, 3622–3629.

(41) Rao, R. P.; Adams, S. Studies of Lithium Argyrodite Solid Electrolytes for All-Solid-State Batteries. *Physica Status Solidi (A) Applications and Materials Science*. 2011, pp 1804–1807.

(42) Chen, M.; Adams, S. High Performance All-Solid-State Lithium/Sulfur Batteries Using Lithium Argyrodite Electrolyte. *J. Solid State Electrochem.* **2015**, *19*, 697–702.

(43) Koerver, R.; Aygün, I.; Leichtweiß, T.; Dietrich, C.; Zhang, W.; Binder, J. O.; Hartmann, P.; Zeier, W. G.; Janek, J. Capacity Fade in Solid-State Batteries: Interphase Formation and Chemomechanical Processes in Nickel-Rich Layered Oxide Cathodes and Lithium Thiophosphate Solid Electrolytes. *Chem. Mater.* **2017**, *29*, 5574–5582.

(44) Sakuda, A.; Hayashi, A.; Tatsumisago, M. Sulfide Solid Electrolyte with Favorable Mechanical Property for All-Solid-State Lithium Battery. *Sci. Rep.* **2013**, *3*, 2261.

(45) De Klerk, N. J. J.; Rosłoń, I.; Wagemaker, M. Diffusion Mechanism of Li Argyrodite Solid Electrolytes for Li-Ion Batteries and Prediction of Optimized Halogen Doping: The

Effect of Li Vacancies, Halogens, and Halogen Disorder. *Chem. Mater.* **2016**, *28*, 7955–7963.

(46)   Bernges, T.; Culver, S. P.; Minafra, N.; Koerver, R.; Zeier, W. G. Competing Structural Influences in the Li Superionic Conducting Argyrodites $Li_6PS_{5-x}Se_xBr$ ($0 \leq x \leq 1$) upon Se Substitution. *Inorg. Chem.* **2018**, *57*, 13920–13928.

(47)   Kong, S. T.; Gün, Ö.; Koch, B.; Deiseroth, H. J.; Eckert, H.; Reiner, C. Structural Characterisation of the Li Argyrodites Li_7PS_6 and Li_7PSe_6 and Their Solid Solutions: Quantification of Site Preferences by MAS-NMR Spectroscopy. *Chem. - A Eur. J.* **2010**, *16*, 5138–5147.

(48)   Wang, Y.; Richards, W. D.; Ong, S. P.; Miara, L. J.; Kim, J. C.; Mo, Y.; Ceder, G. Design Principles for Solid-State Lithium Superionic Conductors. *Nat. Mater.* **2015**, *14*, 1026–1031.

(49)   Krauskopf, T.; Pompe, C.; Kraft, M. A.; Zeier, W. G. Influence of Lattice Dynamics on Na^+ Transport in the Solid Electrolyte $Na_3PS_{4-x}Se_x$. *Chem. Mater.* **2017**, *29*, 8859–8869.

(50)   Krauskopf, T.; Muy, S.; Culver, S. P.; Ohno, S.; Delaire, O.; Shao-Horn, Y.; Zeier, W. G. Comparing the Descriptors for Investigating the Influence of Lattice Dynamics on Ionic Transport Using the Superionic Conductor $Na_3PS_{4-x}Se_x$. *J. Am. Chem. Soc.* **2018**, *140*, 14464–14473.

(51)   Muy, S.; Bachman, J. C.; Giordano, L.; Chang, H. H.; Abernathy, D. L.; Bansal, D.; Delaire, O.; Hori, S.; Kanno, R.; Maglia, F.; Lupart, S.; Lamp, P.; Shao-Horn, Y. Tuning Mobility and Stability of Lithium Ion Conductors Based on Lattice Dynamics. *Energy Environ. Sci.* **2018**, *11*, 850–859.

(52)   Rice, M. J.; Roth, W. L. Ionic Transport in Super Ionic Conductors: A Theoretical Model. *J. Solid State Chem.* **1972**, *4*, 294–310.

(53)   Vineyard, G. H. Frequency Factors and Isotope Effects in Solid State Rate Processes. *J. Phys. Chem. Solids* **1957,** *3*, 121−127.

(54)   Brüesch, P.; Pietronero, L.; Strässler, S.; Zeller, H. R. Brownian Motion in a Polarizable Lattice: Application to Superionic Conductors. *Phys. Rev. B* **1977**, *15*, 4631–4637.

(55)   Hanghofer, I.; Gadermaier, B.; Wilkening, H. M. R. Fast Rotational Dynamics in Argyrodite-Type Li_6PS_5X (X: Cl, Br, I) as Seen by 31P Nuclear Magnetic Relaxation - On Cation-Anion Coupled Transport in Thiophosphates. *Chem. Mater.* **2019**, *31*, 4591–4597.

(56)   Coelho, A. A. TOPAS and TOPAS-Academic: An Optimization Program Integrating Computer Algebra and Crystallographic Objects Written in C++: An. *J. Appl.*

Crystallogr. **2018**, *51*, 210–218.

(57) Shannon, R. D. Revised Effective Ionic Radii and Systematic Studies of Interatomie Distances in Halides and Chaleogenides Bond Strength-Bond Length Relationships , and Plots of (1) Radii vs Volume , (2) Radii vs Coordination Partial Occupancy of Cation Sites , Coval. *Acta Crystallogr.* **1976**, *A32*, 751.

(58) Denton, A. R.; Ashcroft, N. W. Vegards Law. *Phys. Rev. A* **1991**, *43*, 3161–3164.

(59) Epp, V.; Gün, Ö.; Deiseroth, H. J.; Wilkening, M. Long-Range Li+ Dynamics in the Lithium Argyrodite Li_7PSe_6 as Probed by Rotating-Frame Spin-Lattice Relaxation NMR. *Phys. Chem. Chem. Phys.* **2013**, *15*, 7123–7132.

(60) Sagotra, A. K.; Chu, D.; Cazorla, C. Influence of Lattice Dynamics on Lithium-Ion Conductivity: A First-Principles Study. *Phys. Rev. Mater.* **2019**, *3*, 035405.

(61) Rao, M. N.; Goel, P.; Choudhury, N.; Chaplot, S. L., Subrata, G. Lattice Dynamics and Inelastic Neutron Scattering Experiments on andalusite, Al_2SiO_5 *.Solid State Comm.* **2002**, *121*, 333-338.

(62) Kolev, N.; Bontchev, R. P.; Jacobson, A. J.; Popov, V. N.; Hadjiev, V. G.; Litvinchuk, A. P.; Iliev, M. N. Raman Spectroscopy of $CaCu_3Ti_4O_{12}$. *Phys. Rev. B*, **2012**, *66*, 132102.

(63) Stirling, W. G. Neutron Inelastic Scattering Study of the Lattice Dynamics of Strontium Titanate: Harmonic Models. *J. Phys. C Solid State Phys.* **1972**, *5*, 2711–2730.

(64) Sturhahn, W.; Toellner, T.S.; Alp, E. E.; Zhang, X.; Ando, M.; Yoda, Y.; Kikuta, S.; Seto, M.; Kimball, C. W.; Dabrowski, B. Phonon Density of States Measured by Inelastic Nuclear Resonant Scattering. *Phys. Rev.* **1958**, *74*, 326–328.

(65) Agne, M. T.; Hanus, R.; Snyder, G. J. Minimum Thermal Conductivity in the Context of: Diffuson -Mediated Thermal Transport. *Energy Environ. Sci.* **2018**, *11*, 609–616.

(66) West, A.; Irvine, J.; Sinclair, D. Electroceramics : Characterization by Impedance Spectroscopy. *Adv. Mater.* **1990**, *2*, 132–138.

(67) Weiss, M.; Weber, D. A.; Senyshyn, A.; Janek, J.; Zeier, W. G. Correlating Transport and Structural Properties in $Li_{1+x}Al_xGe_{2-x}(PO_4)_3$ (LAGP) Prepared from Aqueous Solution. *ACS Appl. Mater. Interfaces* **2018**, *10*, 10935–10944.

(68) Mariappan, C. R.; Yada, C.; Rosciano, F.; Roling, B. Correlation between Micro-Structural Properties and Ionic Conductivity of $Li_{1.5}Al_{0.5}Ge_{1.5}(PO_4)_3$ Ceramics. *J. Power Sources* **2011**, *196*, 6456–6464.

(69) Brug, G. J.; van den Eeden, A. L. G.; Sluyters-Rehbach, M.; Sluyters, J. H. The Analysis of Electrode Impedances Complicated by the Presence of a Constant Phase Element. *J. Electroanal. Chem.* **1984**, *176*, 275–295.

For table of contents only

8.25x4.45 cm is the limit